CD36-Pyruvate Kinase M2 Signaling Promotes Macrophage Phagocytosis Through Mitochondrial Reactive Oxygen Species

*[1]Jue Zhang, [1]Jackie Chang, [1]Vaya Chen, [1]Mirza Ahmar Beg, [1]Wenxin Huang, [2]Lance Vick, [1]Heng Zhang, [3]Ankan Gupta, [1]Mark Castleberry, [1]Ziyu Zhang, [1]Wen Dai, [1]Jieqing Zhu, [4]Moua Yang, [5,6]Ashley Kaye Brown, [1]Zhen Xu, [1,2]Yan-Qing Ma, [2]Brian C. Smith, [7]Jacek Zielonka, [6]Weiguo Cui, [1,8]Ze Zheng, *[1,8]Yiliang Chen

[1]Versiti Blood Research Institute, Milwaukee, WI 53226

[2]Department of Biochemistry, Medical College of Wisconsin, Milwaukee, WI 53226

[3]Department of Pediatrics, Medical College of Wisconsin, Milwaukee, WI 53226

[4]Division of Hemostasis and Thrombosis, Beth Israel Deaconess Medical Center and Harvard University, Boston, MA 02215

[5]Department of Microbiology and Immunology, Medical College of Wisconsin, Milwaukee, WI 53226

[6]Department of Pathology, Northwestern University, Chicago, IL, 60611

[7]Department of Biophysics, Medical College of Wisconsin, Milwaukee, WI 53226

[8]Department of Medicine, Medical College of Wisconsin, Milwaukee, WI 53226

Short title: CD36-PKM2 Promotes Phagocytosis Through mtROS

**To whom correspondence should be addressed:*

Yiliang Chen, Ph.D. Telephone: 414-937-3811; E-mail: yilchen@mcw.edu

Jue Zhang, M.D., Ph.D. Telephone: 414-937-6808; E-mail: juezhang@versiti.org

Address: 8701 Watertown Plank Rd. Milwaukee, WI, 53226

Word count: 8181

23 **ABSTRACT**

24 **OBJECTIVE:** Macrophage phagocytosis function is critical for tissue homeostasis, but excessive
25 phagocytosis leads to lipid overloading and foam cell formation, a hallmark of atherosclerosis.
26 However, regulatory mechanisms of phagocytosis under atherogenic conditions remain poorly
27 understood. We previously reported that macrophage oxLDL/CD36 signaling drives
28 mitochondrial reactive oxygen species (mtROS) production during atherosclerosis initiation. Here
29 we aim to determine the role of CD36-mtROS axis in regulation of phagocytosis and explore the
30 underlying molecular mechanism, which could provide new potential therapeutic targets.

31 **METHODS AND RESULTS:** Feeding macrophages with a variety of large particles including
32 pHrodo-conjugated E.coli, green fluorescence beads, and fluorescence-labeled apoptotic cells, we
33 showed that oxLDL upregulated phagocytosis efficiency in macrophages. This effect was
34 dependent on CD36 as it was attenuated in *Cd36*-null macrophages. Through use of mtROS
35 scavenger MitoTEMPO, MCAT transgenic strategy and antioxidant signaling stimulation, we
36 observed that mtROS were required for oxLDL-upregulated phagocytosis. Using the
37 atherosclerosis-prone *Apoe*-null mouse model, we found that aortic foamy macrophages displayed
38 both elevated levels of mtROS and phagocytosis functions during the initiation of atherosclerosis.
39 Employing a combination of co-immunoprecipitation, mass spectrometry, genetic knockdown by
40 siRNA, and small chemical inhibitors, we identified a cytosolic enzyme PKM2 downstream of
41 oxLDL/CD36 signaling, which translocated to the mitochondria with the assistance of a chaperone
42 GRP75. Subsequently, mitochondrial PKM2 bound to the electron transport chain Complex III,
43 potentially facilitating mtROS production.

44 **CONCLUSIONS:** These findings reveal a novel CD36-PKM2-mtROS pathway in macrophages
45 that could lead to excess phagocytosis during the initiation of atherosclerosis.

Keywords: CD36, PKM2, Phagocytosis, Mitochondria, ROS

Non-Standard Abbreviations and Acronyms: AC: apoptotic cell bodies; **2-DG**: 2-deoxy-D-glucose; **ETC**: electron transport chain; **FSC**: forward scatter; **HFD**: high fat diet; **HMDM**: human monocyte-derived macrophages; **IP**: immunoprecipitation; **MCAT**: mitochondrial-targeted human catalase expression; **MFI**: mean fluorescence intensity; **mtROS**: mitochondrial reactive oxygen species; **oxLDL**: oxidized low-density lipoprotein; **PKM2**: pyruvate kinase muscle 2; **PLA**: proximity ligation assay; **RT**: room temperature; **scRNA-seq**: single-cell RNA sequencing; **Trem2**: triggering receptor expressed on myeloid cells 2; **TUNEL**: terminal deoxynucleotidyl transferase dUTP nick end labeling; **UMAP**: uniform manifold approximation and projection; **WT**: wild type;

56 **INTRODUCTION**

57 Macrophages eliminate pathogens, apoptotic cell bodies, and cell debris through phagocytosis,
58 which is critical in maintaining tissue homeostasis. However, overstimulation of phagocytosis
59 imposes a heavy metabolic burden on macrophages and leads to intracellular lipid accumulation
60 and foam cell formation[1, 2], a hallmark of initiation of atherosclerosis. Lipoproteins retained in the
61 arterial subendothelial space are modified into atherogenic particles including oxidized LDL
62 (oxLDL), which binds to macrophage surface receptors such as CD36, promoting intracellular
63 lipid accumulation and foam cell formation[3, 4]. Despite a well-recognized role as a proatherogenic
64 lipoprotein complex, the effects of oxLDL on macrophage phagocytosis functions and underlying
65 molecular mechanisms are largely unknown.

66 We previously reported that oxLDL/CD36 signaling reprogrammed macrophage
67 metabolism from mitochondrial respiration to glycolysis with alterations in mitochondrial
68 phenotypes such as an increase in fission and production of mitochondrial reactive oxygen species
69 (mtROS)[5]. Using a diet-induced atherosclerosis mouse model (*Apoe*-null[6]), we further showed that
70 mtROS levels were continuously elevated in circulating monocytes in a CD36-dependent manner
71 during the initiation of atherosclerosis. Mitochondrial dysfunction is often associated with
72 atherosclerosis in both animal models and human patients[7]. Suppressing mtROS using a transgenic
73 strategy (mitochondrial-specific human catalase overexpression, or MCAT) appeared to protect
74 mice from early atherogenesis[8], indicating a contributing role of mtROS. While we and others
75 have revealed connections of mtROS to pro-inflammatory signaling such as the NF-κB pathway
76 and the pro-inflammatory cytokine productions[5, 8], two important questions remain to be addressed:
77 1. Do mtROS affect the macrophage cellular functions, and 2. What is the mechanism of mtROS
78 induction.

79 In this study, we first showed that oxLDL upregulated phagocytosis efficiency using: 1.
80 pHrodo-conjugated bioparticles; 2. Green fluorescence beads; and 3. Fluorescence-labeled
81 apoptotic cells. Next, using *Cd36*-null macrophages, we observed that the oxLDL effect on
82 phagocytosis was CD36-dependent. Then, using three complementary strategies to reduce mtROS
83 levels including mtROS scavenger, MCAT transgenic models, and small chemical compounds
84 stimulating antioxidant pathways, we showed that oxLDL/CD36 axis promoted phagocytosis
85 through mtROS. Moreover, we provided *in vivo* evidence showing that elevated mtROS were
86 associated with increased phagocytosis efficiency in aortic foamy macrophages during the
87 initiation of atherosclerosis. Mechanistically, oxLDL/CD36 signaling triggered the translocation
88 of a glycolytic enzyme pyruvate kinase muscle 2 (PKM2) from cytosol to the mitochondria, which
89 is assisted by the chaperone protein GRP75. The mitochondrial PKM2 then binds to the electron
90 transfer chain (ETC) Complex III, which may induce leakage of the electron leading to mtROS
91 induction. These findings define a novel oxLDL-CD36-PKM2-mtROS pathway in macrophages
92 and reveal a regulatory role of mtROS in phagocytosis during the initiation of atherosclerosis.

93 **METHODS**

94 **Data Availability**

95 The authors declare that all supporting data and methods are available within the article and the
96 Supplemental Materials. The Major Resources Table is included in the Supplemental Materials.
97 Additional supporting data and methods are available from the corresponding authors upon
98 reasonable request.

99 ***In Vitro* Phagocytosis Assays**

100 Cells were seeded into 6-well plates at 0.25 X 10^6 cells/well and treated with oxLDL. To determine
101 the phagocytosis efficiency of macrophages, cells were incubated with 20 μg/ml pHrodo-

102 conjugated *E. coli* bioparticles for 30min. Cells were washed with PBS twice to remove free
103 bioparticles, lifted by scraping and suspended for flow cytometry analysis using the fluorescein
104 isothiocyanate (FITC) channel.

105 ***In Vitro* Macrophage mtROS Measurements**

106 Cells were seeded into 6-well plates at 0.25 X 10^6 cells/well. After treatment, cells were incubated
107 with 5 μM MitoNeoD for 15min. Cells were washed with PBS twice, lifted by scraping, and
108 suspended for flow cytometry analysis using the phycoerythrin (PE) channel.

109 ***Ex Vivo* Aortic F4/80$^+$/Trem2$^+$ Macrophage mtROS Assays and Phagocytosis Assays**

110 Mice were sacrificed after 6 weeks of chow/HFD. The whole aortas were removed, digested in
111 gentle MACS™ C Tubes (Miltenyi Biotec) with an enzyme mixture (Liberase, 0.77 mg/ml;
112 Hyaluronidase, 0.3 mg/ml; Deoxyribonuclease, 0.3 mg/ml; BSA, 1mg/ml; $CaCl_2$, in PBS) by a
113 gentle MACS™ Octo Dissociator with Heaters (Miltenyi Biotec) at 37°C for 45 min. Cell
114 suspension was then filtered by a 40 μm cell strainer to remove the large debris. For mtROS assays,
115 the filtered single-cell suspension was incubated with 5 μM MitoNeoD in RPMI1640 with 10%
116 FBS at 37°C for 15 min, followed by immunostaining with Pacific Blue-conjugated F4/80
117 antibody (BioLegend, Cat#123123) and APC-conjugated Trem2 antibody (R&D Systems,
118 Cat#FAB17291A) in Flow Buffer at room temperature (RT) for 15 min in the dark. Cells were
119 then washed once with Flow Buffer and resuspended in 200 μl Flow Buffer for flow cytometry
120 analysis. For phagocytosis assays, the filtered single-cell suspension was incubated with 20 μg/ml
121 pHrodo-conjugated *E. coli* bioparticles in RPMI1640 with 10% FBS at 37°C for 30 min, followed
122 by immunostaining with PE/Cy5-conjugated F4/80 antibody (BioLegend, Cat#123111) and PE-
123 conjugated Trem2 antibody (R&D Systems, Cat#FAB17291P) in Flow Buffer at RT for 15 min in

124 the dark. Cells were then washed once with Flow Buffer and resuspended in 200 µl Flow Buffer
125 for flow cytometry analysis.

126 ***In Vivo* Aortic F4/80$^+$/Trem2$^+$ Macrophage Phagocytosis Assays**

127 At 6-week on chow/HFD, each mouse was injected with 50 µg pHrodo-conjugated *E. coli*
128 bioparticles through the tail vein. 3 h later, mice were sacrificed and the aortas were processed as
129 described in the *ex vivo* phagocytosis assay. The pHrodo bioparticle incubation step was skipped.

130 ***In Vitro* Efferocytosis Assays**

131 To generate apoptotic cell bodies (AC), WT murine peritoneal macrophages were treated with 50
132 µg/ml oxLDL for 48 h. Apoptosis was confirmed by PE-conjugated Annexin V binding assay. AC
133 were lifted by scraping and labeled with a green fluorescent dye PKH67. PKH67-labeled AC were
134 then incubated with macrophages with the ratio of AC: macrophages (4:1) in the cell culture
135 incubator for 15 min. Unbound AC were washed away by PBS for three times. Then macrophages
136 were lifted by scraping, suspended in the Flow Buffer and subjected to flow cytometry analysis
137 using the FITC channel.

138 ***In Vivo* Efferocytosis Assays**

139 The assays were conducted based on a previously established protocol[9, 10]. Briefly, WT and their
140 litter mate MCAT mice were intraperitoneally injected with dexamethasone (250 µg per mouse
141 dissolved in 1ml PBS). 20 h after injection, mice were euthanized, and thymuses were harvested.
142 Then thymuses were briefly rinsed in PBS and disaggregated by mechanical forces. The cell
143 suspension was filtered by a 40 µm cell strainer to remove the large debris. The thymocytes were
144 subsequently stained with TUNEL assay kit substrate (Abcam, Cat#ab66110) and FITC-
145 conjugated F4/80 antibody (BioLegend, Cat#123107) at RT for 15 min in the dark. Cells were then
146 washed once with Flow Buffer and resuspended in 200 µl Flow Buffer for flow cytometry analysis.

147 **Immunoprecipitation and Immunoblot Analysis**

148 Cells were washed with PBS and lysed with ice-cold CelLytic M Cell Lysis Reagent containing
149 protease inhibitor cocktail (Roche) and phosphatase inhibitors (Sigma). For immunoprecipitation
150 assays, the lysates were pre-cleared with A/G agarose beads (Thermo Scientific) at 4°C for 1 h.
151 The supernatants containing the same amount of protein (~1 mg) were incubated with 10 µl
152 primary antibody overnight at 4°C; 25 µl of A/G agarose beads was then added and incubated
153 overnight at 4°C. The beads were washed, boiled in loading buffer and the supernatant was loaded
154 to SDS-PAGE gel. The signals were detected with chemiluminescent substrate (Thermo Scientific)
155 and quantified by ImageJ software. For immunoblotting, protein concentrations were determined
156 by the NanoDrop One/OneC spectrophotometer (Thermo Scientific) and equal amounts of proteins
157 were loaded in each lane.

158 **Immunofluorescence Assay**

159 Macrophages were seeded on uncoated glass coverslips and fixed in 4% paraformaldehyde for 15
160 min, permeabilized in 0.2% Triton X-100 for 10 min and blocked with 3% BSA for 1h. The cells
161 were incubated with primary antibodies overnight at 4°C and then fluorescence-conjugated
162 secondary antibodies for 3 h at RT in the dark. Cells were then washed and counterstained with
163 4',6-diamidino-2-phenylindole (DAPI) Vectashield mounting medium and imaged by laser
164 confocal fluorescence microscopy (Olympus).

165 ***In-Situ* Proximity Ligation Assay (PLA)**

166 Macrophages were fixed and incubated with rabbit anti-PKM2 (Cell Signaling, Cat#4053) and
167 mouse anti-UQCRC1 monoclonal antibodies (Invitrogen, Cat#459140). Cells were then washed
168 and incubated with species-specific secondary antibodies (Olink) conjugated to unique DNA
169 strands. Negative control slides were only incubated with secondary antibodies. The

170 oligonucleotides and a ligase were added to form a circular template which was then amplified and
171 detected using complementary fluorescently labeled probes. Red fluorescent dots representing
172 protein-protein interaction were visualized by laser confocal fluorescence microscope[11].

173 **Statistics**

174 Data are presented as means ± standard error of the mean (SEM) and all statistical analysis was
175 done using GraphPad Prism 9 software. D'Agostino-Pearson omnibus normality test was
176 performed to confirm that data are normally distributed followed by the Student's t test (two-tailed,
177 unpaired, and equal variance) for comparisons between two groups. For data comparison involving
178 more than two groups, ANOVA followed by Dunnett's or Tukey's multiple comparisons test.
179 Statistical values, including number of replicates (n), are noted in the figure legends. In all figures,
180 "ns" means not significant. *P<0.05, **P<0.01, ***P<0.001, ****P<0.0001. For *in vitro* studies
181 n=number of biological repeats while for the *in vivo* studies, n=number of animals.

182

183 **RESULTS**

184 **OxLDL Stimulates CD36-Dependent Phagocytosis in Macrophages.**

185 We pre-treated wild-type (WT) murine peritoneal macrophages with 20 μg/ml oxLDL for 24 h,
186 followed by incubation with pHrodo-conjugated *E. coli* bioparticles for 30 min. As pHrodo is non-
187 fluorescent outside the cell at neutral pH but gives bright fluorescence in the phagolysosomes with
188 an acidic pH environment, pHrodo fluorescence intensity was detected and quantified by flow
189 cytometry to be used as a phagocytosis efficiency indicator[12]. OxLDL stimulated 87% higher
190 phagocytosis efficiency (Figure 1A). However, the non-oxidized LDL or HDL did not increase
191 phagocytosis, indicating that oxLDL-stimulation in phagocytosis is not a general effect of
192 lipoproteins. Similarly, oxLDL stimulated a 33% higher phagocytosis efficiency in human

193 monocyte-derived macrophages (HMDMs) (Figure 1B). To corroborate, we next showed that
194 oxLDL stimulated phagocytosis in a dose- (Figure 1C) and time-dependent (Figure 1D) manner.
195 A significant 24% stimulation was observed as short as 5 h after oxLDL treatment. The oxLDL
196 effect was not limited to the phagocytosis of *E. coli* bioparticles because oxLDL also stimulated
197 the phagocytosis of polystyrene beads (Figure S1A). Since polystyrene beads did not contain
198 bacteria surface antigens such as LPS, this result suggested that the oxLDL phagocytosis-
199 stimulating effect was not mediated by LPS/TLR4 signaling. As a validation, the phagocytosis-
200 stimulating effect was observed in *Tlr4*-null macrophages, similar to WT macrophages (Figure
201 S1B). Instead, oxLDL-induced phagocytosis was attenuated in *Cd36*-null macrophages (Figure
202 1E), indicating that this effect involves CD36. CD36 is known to facilitate phagocytosis by direct
203 interaction and recognition of bioparticles[13], and oxLDL can upregulate CD36 expression in
204 macrophages[14]. So, we next tested whether oxLDL-induced phagocytosis was due to more
205 macrophage-*E. coli* binding by co-incubation at 4°C. However, we did not detect a significant
206 increase in macrophage-*E. coli* binding after oxLDL pre-treatment of either murine peritoneal
207 macrophages (Figure S1C) or HMDMs (Figure S1D). Additionally, as oxLDL still increased
208 phagocytosis, although to a less extent, in *Cd36*-null macrophages (Figure 1E), this effect was
209 unlikely mediated through direct interaction between macrophage surface CD36 and bioparticles.
210 Thus, we reasoned that an intracellular event downstream of oxLDL/CD36 axis contributed to the
211 oxLDL-stimulated phagocytosis.

212 **OxLDL-Induced Phagocytosis Is Dependent on Mitochondrial Reactive Oxygen Species**
213 **(mtROS).** We reported previously that oxLDL increased mtROS levels through CD36 in
214 macrophages[5]. To test whether mtROS are involved in oxLDL-induced phagocytosis, we co-
215 stained macrophages with MitoNeoD, a specific mitochondria-targeted fluorescent superoxide

216 radical anion probe [5, 15], and pHrodo-conjugated *E. coli* bioparticles. OxLDL pre-treatment led to
217 a significant increase in a macrophage subpopulation high in both mtROS and pHrodo signals
218 (Figure 2A), which indicated that mtROS levels were positively correlated with phagocytosis
219 efficiency. Moreover, MitoTEMPO, a mtROS scavenger, fully blocked oxLDL-induced
220 phagocytosis (Figure 2B) without affecting *E. coli* and macrophage binding (Figure S1C), which
221 indicated that mtROS promote macrophage uptake but not recognition of the bioparticles. To
222 validate, we used peritoneal macrophages from MCAT mice, which overexpress human catalases
223 in the mitochondria, suppressing mtROS[8]. Consistently, MCAT macrophages were resistant to
224 oxLDL stimulation in phagocytosis, although the basal phagocytosis efficiency was not affected
225 (Figure 2C). There was also no difference in the binding of *E. coli* bioparticles to WT or MCAT
226 macrophages (Figure S1E).

227 Cellular redox status is regulated by a deacetylase Sirt1, the activation of which suppresses
228 mtROS production in macrophages[16, 17]. To confirm that the pro-oxidant status was responsible
229 for oxLDL-stimulated phagocytosis, we used SRT1720, an agonist of Sirt1[18], and showed that
230 SRT1720 significantly reduced both mtROS (Figure 2D) and phagocytosis (Figure 2E) as induced
231 by oxLDL. To rule out the possibility that the phagocytosis induction was a secondary
232 compensatory effect of mitochondrial dysfunction in response to oxLDL, we used various electron
233 transport chain (ETC) inhibitors including rotenone (Complex I), antimycin (Complex III),
234 oligomycin (Complex V), and FCCP (uncoupler of oxidative phosphorylation). None of the ETC
235 inhibitors resulted in increased phagocytosis in macrophages (Figure S2A). Therefore, we
236 concluded that macrophages actively upregulate mtROS levels to facilitate phagocytosis in
237 response to oxLDL. However, using mitochondrial-targeted redox cycler Mito-Paraquat-derived[19]
238 compounds MitoNP, we showed that, although MitoNP promoted mtROS in macrophages (Figure

239 S2B), it inhibited instead of stimulating phagocytosis (Figure S2C). Thus, mtROS alone are not
240 sufficient to increase phagocytosis efficiency in macrophages, although they are required for
241 oxLDL-induced phagocytosis.

242 **Aortic F4/80$^+$/Trem2$^+$ Macrophages Show Increased Phagocytosis Efficiency Dependent on**
243 **CD36 During Initiation Stages of Atherosclerosis.** OxLDL promotes foam cell formation and
244 facilitates the initiation and development of atherosclerosis[3, 4, 20]. We reported that mtROS were
245 continuously elevated in circulating white blood cells, among which were Ly6C^{high}
246 proinflammatory monocytes during the initiation stages of atherogenesis in *Apoe*-null mice fed
247 with HFD up to 6 weeks[5]. Ly6C^{high} proinflammatory monocytes constitute a major subpopulation
248 that infiltrates the lesion sites and gives rise to plaque macrophages[21, 22]. Thus, we next investigated
249 the mtROS-phagocytosis axis in the aortic lesional macrophages. For *ex vivo* experiments, *Apoe*-
250 null or *Apoe/Cd36* double-null mice were fed with chow diet or HFD for 6 weeks and the aorta
251 were dissected, digested to single-cell suspension, and stained with anti-F4/80 (macrophage
252 marker), anti-Trem2 (aortic foam cell marker)[23], MitoNeoD, and *E. coli*-pHrodo (Figure 3A).
253 Clumped cells were excluded for analysis using the FSC-A vs. FSC-H gating strategy(Figure S3A).
254 As expected, we found that HFD led to increased aortic F4/80$^+$ macrophages (Figure S3B) as well
255 as an 81% increase in F4/80$^+$/Trem2$^+$ aortic foamy macrophages in *Apoe*-null mice (Figure 3B).
256 Interestingly, the amounts of F4/80$^+$/Trem2$^+$ aortic foamy macrophages were decreased in
257 *Apoe/Cd36* double-null mice under both chow and HFD conditions (Figure 3B), consistent with a
258 previous report that *Apoe/Cd36* double-null mice were protected from HFD-induced
259 atherosclerosis[24]. 6-week of HFD led to a 53% increase in mtROS levels in F4/80$^+$/Trem2$^+$ aortic
260 foamy macrophages from *Apoe*-null mice. However, HFD-induced mtROS were not observed in
261 F4/80$^+$/Trem2$^+$ aortic foamy macrophages from *Apoe/Cd36* double-null mice (Figure 3C),

262 suggesting that CD36 is required for mtROS induction under atherogenic conditions. Moreover,
263 HFD led to a 25% increase in phagocytosis efficiency in F4/80^{+}/Trem2^{+} aortic foamy macrophages
264 from *Apoe*-null mice, but not in those from *Apoe/Cd36* double-null mice (Figure 3D).

265 We consolidated the *ex vivo* results by conducting an *in vivo* phagocytosis assay. We
266 injected *E. coli*-pHrodo through tail veins, waited for 3h, and collected mouse aorta for FACS
267 analysis on F4/80^{+}/Trem2^{+} macrophages (Figure 3E). Consistently, phagocytosis efficiency
268 increased 52% by HFD in *Apoe*-null mice but no significant difference was observed in *Apoe/Cd36*
269 double-null mice or in *Apoe*-null/MCAT mice (Figure 3F). Moreover, the HFD-stimulated
270 phagocytosis effect was only displayed in F4/80^{+}/Trem2^{+} macrophages from aorta but not from
271 other tissues including adipose tissue and liver (Figure S3C). Additionally, there was no detectable
272 pHrodo signal from peripheral blood monocytes (data not shown). Thus, induction of mtROS
273 contributed to an increase in phagocytosis efficiency in F4/80^{+}/Trem2^{+} aortic foamy macrophages
274 in a CD36-dependent manner during the initiation of atherosclerosis.

275 **OxLDL Stimulates Efferocytosis through CD36 and MtROS Signaling.** Efferocytosis, the
276 process by which phagocytes ingest apoptotic cell bodies (AC), is a sub-type of phagocytosis,
277 which is one of the major macrophage functions for tissue homeostasis[25]. To generate AC for the
278 *in vitro* efferocytosis assay, we used two different AC models. Firstly, high doses of oxLDL are
279 known to cause macrophage apoptosis *in vitro*[26, 27]. In agreement with the literature, we found that
280 50 μg/ml oxLDL treatment for 48h led to apoptosis in macrophages (Figure S4A). We collected
281 oxLDL-induced AC, labeled with PKH67, a green fluorescence dye that inserts and labels AC
282 membranes, and co-incubated with macrophages pre-treated with 20 μg/ml of different
283 lipoproteins. Unbound AC were washed away after 15min incubation and PKH67 fluorescence in
284 live macrophages was quantified by flow cytometry as an indicator of efferocytosis efficiency.

285 Consistent with phagocytosis (Figure 1), oxLDL, but not LDL or HDL, stimulated efferocytosis
286 efficiency (Figure S4B and Video S1/S2). OxLDL-stimulated efferocytosis was dose- (Figure S4C)
287 and time-dependent (Figure S4D). In a second AC model, we used murine neutrophils isolated
288 from whole blood, and allowed them to undergo spontaneous apoptosis before labeling them with
289 PKH67 for the *in vitro* efferocytosis assay. Consistently, oxLDL increased macrophage
290 efferocytosis of neutrophil AC (Figure S4E).

291 Compared to WT peritoneal macrophages, *Cd36*-null macrophages displayed comparable
292 efferocytosis efficiency at the basal level (control condition) but showed less induction in
293 efferocytosis (Figure 4A). Moreover, both MitoTEMPO and the MCAT transgenic strategy
294 significantly inhibited oxLDL-stimulated efferocytosis (Figure 4B and 4C). Thus, CD36 and its
295 downstream mtROS induction play critical roles in oxLDL-induced efferocytosis. Interestingly,
296 we found that AC alone induced mtROS production in a subpopulation of macrophages (Figure
297 4D). These data prompted us to test whether mtROS modulate efferocytosis for tissue homeostasis
298 *in vivo*.

299 **MtROS Facilitate Efferocytosis *In Vivo*.** We conducted an *in vivo* efferocytosis assay in mouse
300 thymi using an established protocol[9, 10]. WT and their littermates MCAT mice were injected
301 intraperitoneally with dexamethasone to induce thymocyte apoptosis. Based on our Annexin V
302 binding assay, while dexamethasone significantly increased apoptotic cell rates, no difference was
303 observed comparing between WT and MCAT thymocytes (Figure 4E), suggesting that
304 dexamethasone induced a similar amount of AC (apoptotic thymocytes) in WT and MCAT mice
305 thymi. 20h after the injection, we collected mouse thymi and conducted a TUNEL staining to label
306 AC together with F4/80 immuno-staining (macrophage marker) prior to flow cytometry analysis.
307 In PBS (vehicle control)-injected mouse thymi, TUNEL$^+$ AC rates are very low for both WT (1.7%)

308 and MCAT (2.1%) groups (Figure 4F), consistent with the notion that efferocytosis is highly
309 efficient *in vivo* and AC are quickly cleared by surrounding macrophages[25]. Interestingly, while
310 dexamethasone increased TUNEL$^+$ AC rates in both groups, AC rates doubled in MCAT thymi
311 (23.3%) compared to those in WT thymi (10.1%) (Figure 4F). A similar pattern was observed for
312 the free TUNEL$^+$ AC (defined as TUNEL positive but F4/80 negative) rates (Figure 4G), which
313 indicated that suppressed mtROS induction in MCAT led to reduced AC clearance. The difference
314 in AC clearance was unlikely due to different numbers of thymic macrophages as F4/80$^+$ thymic
315 macrophages were comparable between WT and MCAT (Figure 4H). Moreover, it was also
316 unlikely due to less recognition of AC in MCAT thymic macrophages because even more
317 efferocytes (defined as TUNEL$^+$/F4/80$^+$ cells) were observed in dexamethasone-injected MCAT
318 thymuses (Figure 4I). Taken together, our results indicated that mtROS facilitated efferocytosis *in*
319 *vivo*, possibly by stimulating a general phagocytosis efficiency.

320 **OxLDL Induces Pyruvate Kinase Muscle 2 Mitochondrial Translocation, Which Facilitates**
321 **MtROS and Phagocytosis.** Next, we explored the underlying molecular mechanism of oxLDL-
322 induced mtROS, which subsequently facilitated phagocytosis. We hypothesize that a second
323 messenger downstream of the oxLDL/CD36 complex delivers the signal from the cytoplasm into
324 the mitochondria to induce mtROS. We previously demonstrated that oxLDL induced a metabolic
325 switch from mitochondrial oxidative phosphorylation to glycolysis (i.e., glycolytic switch)[5]. To
326 test the potential role of glycolytic switch in mtROS induction, we used the glycolysis inhibitor 2-
327 deoxy-D-glucose (2-DG)[28] and showed that 2-DG significantly blocked both oxLDL-induced
328 mtROS and phagocytosis efficiency (Figure S5A), suggesting that activation of the glycolytic
329 enzymes may be involved. Glycolysis is a series of reactions catalyzed by 10 cytosolic enzymes.
330 If a glycolytic enzyme contributes to mtROS induction under atherogenic conditions, we reason

331 that the expression pattern of that enzyme among different aortic immune cells may be correlated
332 with mtROS levels. Therefore, we re-analyzed the published single-cell RNA sequencing (scRNA-
333 seq) data on $CD45^+$ immune cells isolated from mouse aorta during atherogenesis (*Ldlr*-null on
334 chow or HFD for 11 weeks)[23]. Using the same sets of markers for distinct immune cell sup-types,
335 we identified 11 cell clusters shown by uniform manifold approximation and projection (UMAP)
336 (Figure 5A). The aortic macrophage foam cell population was identified as $Trem2^{high}$ cluster based
337 on the previous studies[23, 29] and shown in the UMAPs (Figure 5A and 5B). Interestingly, the *Pkm*
338 gene, which encodes the last rate-limiting step of the glycolysis, was highly expressed in both
339 $Ly6c^{high}$ pro-inflammatory monocytes and the $Trem2^{high}$ foam cells (Figure 5C and 5D), which
340 was correlated to elevated mtROS levels from the circulating $Ly6c^{high}$ pro-inflammatory
341 monocytes[5] and $F4/80^+/Trem2^+$ aortic foamy macrophages (Figure 3). Nevertheless, genes (i.e.,
342 *Hk1*, *Hk2*, H*k3, Pfkm, Pfkl, Pfkp*) that encode the other two rate-limiting steps of glycolysis showed
343 no such correlation (Figure S5B). Moreover, the *Pkm* highly expressed cells appeared to be
344 predominantly from the HFD-fed mice (Figure 5C and Figure S5C), suggesting upregulation of
345 *pkm* expression in the plaque-forming immune cells during atherogenesis.

346 The gene *pkm* encodes two different isoforms, pyruvate kinase muscle 1 (PKM1) and
347 PKM2, due to RNA splicing. Since oxLDL upregulated PKM2, but not PKM1 (Figure S5D), we
348 then focused on PKM2 in our following mechanistic studies. First, we used siRNA to knockdown
349 PKM2 levels in HMDMs (Figure S5E), which fully blocked oxLDL-induced mtROS and
350 phagocytosis (Figure 5E). PKM2 was reported to translocate to the mitochondria in a human
351 cancer cell line[30]. Thus, we hypothesized that oxLDL induced PKM2 mitochondrial translocation
352 for ROS induction. Supporting the hypothesis, co-staining of both PKM2 and Tom20
353 (mitochondria marker) showed more colocalization of both after oxLDL treatment (Figure 5F). To

354 validate, we used a commercial mitochondrial/cytosol fractionation kit (Thermo Scientific), and
355 the purity of each fraction was confirmed by immunoblot on markers of cytosol, mitochondria,
356 and nuclei (Figure S5F). Next, we showed that oxLDL nearly doubled mitochondrial PKM2 levels
357 in HMDMs, while no change in cytosolic PKM2 levels was observed (Figure 5G). Time course
358 experiments showed that mitochondrial PKM2 levels doubled 1 h after oxLDL treatment, peaked
359 at 3 h, and stayed high up to 24 h (Figure S5G). Moreover, oxLDL-stimulated PKM2
360 mitochondrial translocation was not observed in the *Cd36*-null murine macrophages (Figure 5H),
361 indicating that PKM2 is downstream of oxLDL/CD36 signaling axis. To further test our hypothesis
362 that PKM2 mitochondrial translocation is responsible for oxLDL-induced mtROS, we used the
363 PKM2 targeting inhibitor shikonin[31] and showed that shikonin reduced oxLDL-induced PKM2
364 mitochondrial translocation (Figure 5I), as well as mtROS and phagocytosis (Figure 5J). Taken
365 together, we demonstrate that oxLDL/CD36 signaling stimulates PKM2 translocation to the
366 mitochondria, which induces mtROS facilitating phagocytosis.

367 **GRP75 Mediates PKM2 Translocation to the Mitochondria, Where It Binds to the ETC**
368 **Complex III.** To further understand molecular mechanisms of the PKM2 mitochondrial
369 translocation and its potential targets, we conducted mass spectrometry to identify PKM2
370 interacting proteins. WT peritoneal macrophages were treated with 20μg/ml oxLDL for 3h, lysed,
371 and PKM2 was immunoprecipitated (IP) by a monoclonal rabbit IgG against PKM2. Then, PKM2
372 immunoprecipitates from control and oxLDL-treated cell lysates (n=3) were run on SDS-PAGE,
373 and gel slices were subjected to mass spectrometry to detect proteins that co-IP with PKM2. An
374 irrelevant monoclonal rabbit IgG IP sample and a blank SDS-PAGE gel were used as two negative
375 controls. After eliminating proteins appearing in the negative controls, we identified 26
376 mitochondrial proteins that co-IP with PKM2 (Table. S1).

377 Within the mitochondrial protein list (Table. S1), GRP75 is special because it belongs to
378 the HSP70 family and functions as a chaperone shuttling between cytoplasm and the mitochondria,
379 facilitating the import of cytosolic proteins to the mitochondrial matrix[32, 33]. The mass
380 spectrometry signals of GRP75 in oxLDL-treated PKM2 immunoprecipitates were 3-fold of those
381 from control samples (Table. S1), suggesting an enhanced PKM2/GRP75 interaction in response
382 to oxLDL. We corroborated it with IP PKM2 followed by immunoblot of GRP75 after oxLDL
383 time-course treatment in both murine macrophages and HMDMs. The co-IP results showed that
384 oxLDL significantly enhanced PKM2/GRP75 interaction around 2-3h interval (Figure 6A), while
385 a control IgG antibody did not precipitate either PKM2 or GRP75 (Figure S6A). Additionally,
386 immunostaining showed more colocalization of PKM2 and GRP75 after oxLDL treatment (Figure
387 6B). To test whether GRP75 chaperone function was important for PKM2 mitochondrial
388 translocation, we used a GRP75 selective inhibitor MKT-077[34, 35] and showed that oxLDL-induced
389 PKM2 mitochondrial translocation was blocked by MKT-077 (Figure 6C). Consistently, MKT-
390 077 also significantly inhibited oxLDL-induced phagocytosis (Figure 6D). Furthermore, knocking
391 down GRP75 using siRNA against HSPA9 (the gene encoding GRP75) in HMDMs (Figure S6B)
392 effectively reduced oxLDL-induced phagocytosis (Figure 6E). Taken together, we demonstrate
393 that the chaperone GRP75 facilitates oxLDL-stimulated PKM2 mitochondrial translocation,
394 promoting phagocytosis.

395 ETC Complex III is a major site of electron leakage, leading to mtROS production[36].
396 Interestingly, we identified UQCRC1, a subunit of ETC Complex III exclusively in oxLDL-treated
397 PKM2 immunoprecipitates through mass spectrometry (Table. S1). To validate, we IP PKM2
398 followed by immunoblot of UQCRC1. As expected, more UQCRC1 proteins were detected in
399 PKM2 immunoprecipitates starting 3h and peaking in 24h after oxLDL treatment (Figure 6F).

400 Finally, we performed an *in-situ* proximity ligation assay (PLA) and confirmed the enhanced
401 PKM2/UQCRC1 interaction by oxLDL (Figure 6G). Taken together, we showed that PKM2
402 targets to ETC Complex III, which may provide a potential mechanism for mtROS induction.
403

404 **DISCUSSION**

405 Here, we report *ex vivo* and *in vivo* data showing that CD36 promotes phagocytosis in macrophages
406 through mtROS induction under atherogenic conditions. We further reveal a novel molecular
407 mechanism that oxLDL/CD36 signaling induces translocation of a cytosolic enzyme PKM2 to the
408 mitochondria, where it interacts with the ETC Complex III. The PKM2 mitochondrial
409 translocation is assisted by a chaperone protein GRP75 and is required for mtROS induction by
410 oxLDL/CD36 signaling.

411 We previously showed that oxLDL/CD36 signaling leads to a metabolic reprogramming
412 from mitochondrial respiration to glycolysis, which is accompanied by mtROS induction and pro-
413 atherogenic phenotypes in macrophages[5]. Furthermore, we showed that mtROS are continuously
414 elevated in the circulating monocytes as well as aortic macrophages in a CD36-dependent manner,
415 contributing to the initiation of atherosclerosis[5]. In this study, we took a step further and showed
416 that aortic foamy macrophages (the Trem2^{+} subpopulation[23]) displayed both increased mtROS and
417 phagocytosis efficiency (Figure 3). Since suppressing mtROS using the MCAT transgenic strategy
418 effectively reduced atherosclerosis in mice[8], the results here suggest that mtROS may
419 overstimulate phagocytosis in aortic macrophages, contributing to the initiation of atherosclerosis.
420 Further studies are needed to validate this concept. But at least the evidence clearly supports the
421 concept that macrophage metabolism critically determines its cellular functions such as
422 phagocytosis, which will reciprocally influence cell metabolism as demonstrated by others[37, 38].

423 The finding that mtROS support efficient phagocytosis of AC (efferocytosis) *in vivo*
424 (Figure 4) has emphasized that they have physiological functions[39] and should no longer be
425 considered as evil byproducts of oxidative metabolism. Supporting this notion, we showed here
426 that AC themselves stimulate mtROS in macrophages (Figure 4D). Through an *in vivo*
427 efferocytosis assay, we found that AC were cleared less efficiently in MCAT mice compared to
428 their WT littermates (Figure 4E-4I), which implicates mtROS in tissue homeostasis. Since
429 overproduction of ROS leads to oxidative stress and cytotoxicity, establishing a redox balance may
430 be critical for maintaining cellular and tissue functions. An unresolved question is how AC trigger
431 mtROS in macrophages, which may provide a clue to the redox balance. A previous study has
432 elegantly shown that AC uptake upregulates Drp-1-mediated mitochondrial fission events, which
433 is required for further AC uptake[10]. We published similar observations that oxLDL upregulates
434 Drp-1 and mitochondrial fission[5], which is known to contribute to mtROS induction[40]. Thus, AC
435 may indirectly stimulate mtROS through Drp-1, and oxLDL enhances the impact of AC on mtROS,
436 which tip the balance in favor of more oxidized conditions or even oxidative stress.

437 Emerging evidence indicates that PKM2 is associated with mtROS induction in human
438 patients[41] and contributes to atherogenesis in mice[42]. A recent study has shown that oxLDL
439 stimulates its translocation to the nuclei and promotes aerobic glycolysis and inflammation in
440 macrophages by activating the HIF-1α pathway[43]. Our findings are in agreement with the literature
441 regarding the proatherogenic role of PKM2. OxLDL induces PKM2 mitochondrial translocation
442 and mtROS production (Figure 5), which could further stabilize HIF-1α and drive the metabolic
443 switch to aerobic glycolysis as well as prolonged inflammation. Enhanced interaction between
444 PKM2 and GRP75 and the MKT077 inhibitor studies have partly uncovered the mechanism of
445 how oxLDL/CD36 signaling promotes PKM2 mitochondrial translocation (Figure 6). As PKM2

446 subcellular localization is regulated by its oligomer formation as well as post-translational
447 modifications[44], it would be interesting to further explore CD36 downstream signaling that
448 modifies PKM2 proteins. In fact, we showed here that shikonin, a known PKM2 inhibitor that
449 reduces PKM2 phosphorylation and its dimerization and tetramerization[45, 46], effectively blocked
450 oxLDL-induced PKM2 mitochondrial translocation, mtROS production, and phagocytosis (Figure
451 5I and 5J). These data provide a clue for further exploration of the mechanism how oxLDL/CD36
452 axis regulates mitochondrial functions through glycolysis. In addition, how mitochondrial PKM2
453 induces ROS remains an open question despite our findings that it binds to multiple subunits from
454 the ETC complexes (Table S1). A potential explanation is that PKM2/ETC Complex interaction
455 may induce electron leakage, leading to superoxide generation.

456 Another critical unanswered question is how mtROS promote phagocytosis. As we
457 observed macrophages when they phagocytosed AC using a novel label-free live cell imaging
458 technique, we found that oxLDL pretreatment leads to a highly dynamic and distorted macrophage
459 phenotype (Video S2, highlighted by red arrows) compared to control (Video S1). Those
460 phonotypes may reflect altered actin cytoskeleton dynamics underneath the cell membranes, as
461 rearrangement of the actin filaments drives the phagocytosis process[47]. Moreover, actin can be
462 reversibly modified by ROS, which plays an important role in the regulation of actin filaments[48].
463 OxLDL/CD36 signaling was reported to alter actin dynamics through ROS generation[20]. Thus, we
464 propose that oxLDL/CD36 axis regulates actin rearrangement both temporarily and spatially
465 through fine-tuning of mitochondria fission/fusion events, mtROS induction, and modification of
466 actins or actin-associated motor proteins, which is our ongoing investigation.

467 In summary, we define a novel regulatory mechanism of phagocytosis in proatherogenic
468 macrophages, which provides new therapeutic strategies to balance lipid metabolism and reduce
469 foam cell formation.

470

471 **ACKNOWLEDGMENTS**

472 We thank Dr. Michael P. Murphy (University of Cambridge) and Richard C. Hartley (University
473 of Glasgow) for providing MitoNeoD for mtROS measurements. We thank Ms. Kathryn Williams
474 for her excellent technical support for our mice colony maintenance. Additionally, we appreciate
475 that Dr. Dinesh Jaishanker (Northwestern University) provides the CX-A imaging system and Ms.
476 Justine Johnson (Nanolive SA) helped with the live cell imaging experiments. We also thank our
477 colleagues, Dr. Roy Silverstein, Dr. Daisy Sahoo, and Dr. Mary Sorci-Thomas for their helpful
478 discussion and comments on our work.

479 **SOURCES OF FUNDING**

480 This work was supported by the National Institutes of Health grants (1R01HL164460 to Y. Chen),
481 (5R01HL131836 and 5R01GM137143 to J. Zhu), (1K99HL164888 to M. Yang), (5R01HL160861
482 to Y. Ma), (5R01DK119359 to B.C. Smith), (R01HL163516 to Z. Zheng), American Heart
483 Association Scientist Development Grant (17SDG33661117 to Y. Chen), and Collaborative
484 Sciences Award (to Z. Zheng). It was also funded by the American Society of Hematology Scholar
485 Award (to M. Yang), Eleanor and Miles Shor Award (to M. Yang), Advancing a Healthier
486 Wisconsin Endowment (MCW-Led Seed Grant to Y. Chen), the Medical College of Wisconsin
487 (MCW New Faculty Startup Fund to Y. Chen and Z. Zheng), the Medical College of Wisconsin
488 (CVC Pilot Grant to J. Zhang).

489 **DISCLOSURES**

None.

SUPPLEMENTAL MATERIAL

Supplemental Methods

Table S1

Figure S1-S6

Video S1-S2

Data Set

Major Resources Table

498 **REFERENCE**

499 1. Khoo JC, Miller E, McLoughlin P and Steinberg D. Enhanced macrophage uptake of low
500 density lipoprotein after self-aggregation. *Arteriosclerosis*. 1988;8:348-58.
501 2. De Meyer GR, De Cleen DM, Cooper S, Knaapen MW, Jans DM, Martinet W, Herman
502 AG, Bult H and Kockx MM. Platelet phagocytosis and processing of beta-amyloid precursor
503 protein as a mechanism of macrophage activation in atherosclerosis. *Circ Res*. 2002;90:1197-
504 204.
505 3. Rahaman SO, Lennon DJ, Febbraio M, Podrez EA, Hazen SL and Silverstein RL. A
506 CD36-dependent signaling cascade is necessary for macrophage foam cell formation. *Cell*
507 *Metab*. 2006;4:211-21.
508 4. Chen Y, Kennedy DJ, Ramakrishnan DP, Yang M, Huang W, Li Z, Xie Z, Chadwick
509 AC, Sahoo D and Silverstein RL. Oxidized LDL-bound CD36 recruits an Na(+)/K(+)-ATPase-
510 Lyn complex in macrophages that promotes atherosclerosis. *Sci Signal*. 2015;8:ra91.
511 5. Chen Y, Yang M, Huang W, Chen W, Zhao Y, Schulte ML, Volberding P, Gerbec Z,
512 Zimmermann MT, Zeighami A, Demos W, Zhang J, Knaack DA, Smith BC, Cui W,
513 Malarkannan S, Sodhi K, Shapiro JI, Xie Z, Sahoo D and Silverstein RL. Mitochondrial
514 Metabolic Reprogramming by CD36 Signaling Drives Macrophage Inflammatory Responses.
515 *Circ Res*. 2019;125:1087-1102.
516 6. Nakashima Y, Plump AS, Raines EW, Breslow JL and Ross R. ApoE-deficient mice
517 develop lesions of all phases of atherosclerosis throughout the arterial tree. *Arterioscler Thromb*.
518 1994;14:133-40.
519 7. Madamanchi NR and Runge MS. Mitochondrial dysfunction in atherosclerosis. *Circ Res*.
520 2007;100:460-73.
521 8. Wang Y, Wang GZ, Rabinovitch PS and Tabas I. Macrophage mitochondrial oxidative
522 stress promotes atherosclerosis and nuclear factor-kappaB-mediated inflammation in
523 macrophages. *Circ Res*. 2014;114:421-33.
524 9. Park D, Han CZ, Elliott MR, Kinchen JM, Trampont PC, Das S, Collins S, Lysiak JJ,
525 Hoehn KL and Ravichandran KS. Continued clearance of apoptotic cells critically depends on
526 the phagocyte Ucp2 protein. *Nature*. 2011;477:220-4.

527 10. Wang Y, Subramanian M, Yurdagul A, Jr., Barbosa-Lorenzi VC, Cai B, de Juan-Sanz J,
528 Ryan TA, Nomura M, Maxfield FR and Tabas I. Mitochondrial Fission Promotes the Continued
529 Clearance of Apoptotic Cells by Macrophages. *Cell*. 2017;171:331-345 e22.
530 11. Kennedy DJ, Chen Y, Huang W, Viterna J, Liu J, Westfall K, Tian J, Bartlett DJ, Tang
531 WH, Xie Z, Shapiro JI and Silverstein RL. CD36 and Na/K-ATPase-alpha1 form a
532 proinflammatory signaling loop in kidney. *Hypertension*. 2013;61:216-24.
533 12. Neaga A, Lefor J, Lich KE, Liparoto SF and Xiao YQ. Development and validation of a
534 flow cytometric method to evaluate phagocytosis of pHrodo BioParticles(R) by granulocytes in
535 multiple species. *J Immunol Methods*. 2013;390:9-17.
536 13. Greenberg ME, Sun M, Zhang R, Febbraio M, Silverstein R and Hazen SL. Oxidized
537 phosphatidylserine-CD36 interactions play an essential role in macrophage-dependent
538 phagocytosis of apoptotic cells. *J Exp Med*. 2006;203:2613-25.
539 14. Feng J, Han J, Pearce SF, Silverstein RL, Gotto AM, Jr., Hajjar DP and Nicholson AC.
540 Induction of CD36 expression by oxidized LDL and IL-4 by a common signaling pathway
541 dependent on protein kinase C and PPAR-gamma. *J Lipid Res*. 2000;41:688-96.
542 15. Shchepinova MM, Cairns AG, Prime TA, Logan A, James AM, Hall AR, Vidoni S,
543 Arndt S, Caldwell ST, Prag HA, Pell VR, Krieg T, Mulvey JF, Yadav P, Cobley JN, Bright TP,
544 Senn HM, Anderson RF, Murphy MP and Hartley RC. MitoNeoD: A Mitochondria-Targeted
545 Superoxide Probe. *Cell Chem Biol*. 2017;24:1285-1298 e12.
546 16. Alam F, Syed H, Amjad S, Baig M, Khan TA and Rehman R. Interplay between
547 oxidative stress, SIRT1, reproductive and metabolic functions. *Curr Res Physiol*. 2021;4:119-
548 124.
549 17. Singh CK, Chhabra G, Ndiaye MA, Garcia-Peterson LM, Mack NJ and Ahmad N. The
550 Role of Sirtuins in Antioxidant and Redox Signaling. *Antioxid Redox Signal*. 2018;28:643-661.
551 18. Mitchell SJ, Martin-Montalvo A, Mercken EM, Palacios HH, Ward TM, Abulwerdi G,
552 Minor RK, Vlasuk GP, Ellis JL, Sinclair DA, Dawson J, Allison DB, Zhang Y, Becker KG,
553 Bernier M and de Cabo R. The SIRT1 activator SRT1720 extends lifespan and improves health
554 of mice fed a standard diet. *Cell Rep*. 2014;6:836-43.
555 19. Robb EL, Gawel JM, Aksentijevic D, Cocheme HM, Stewart TS, Shchepinova MM,
556 Qiang H, Prime TA, Bright TP, James AM, Shattock MJ, Senn HM, Hartley RC and Murphy

557 MP. Selective superoxide generation within mitochondria by the targeted redox cycler
558 MitoParaquat. *Free Radic Biol Med*. 2015;89:883-94.
559 20. Park YM, Febbraio M and Silverstein RL. CD36 modulates migration of mouse and
560 human macrophages in response to oxidized LDL and may contribute to macrophage trapping in
561 the arterial intima. *J Clin Invest*. 2009;119:136-45.
562 21. Swirski FK, Libby P, Aikawa E, Alcaide P, Luscinskas FW, Weissleder R and Pittet MJ.
563 Ly-6Chi monocytes dominate hypercholesterolemia-associated monocytosis and give rise to
564 macrophages in atheromata. *J Clin Invest*. 2007;117:195-205.
565 22. Tacke F, Alvarez D, Kaplan TJ, Jakubzick C, Spanbroek R, Llodra J, Garin A, Liu J,
566 Mack M, van Rooijen N, Lira SA, Habenicht AJ and Randolph GJ. Monocyte subsets
567 differentially employ CCR2, CCR5, and CX3CR1 to accumulate within atherosclerotic plaques.
568 *J Clin Invest*. 2007;117:185-94.
569 23. Cochain C, Vafadarnejad E, Arampatzi P, Pelisek J, Winkels H, Ley K, Wolf D, Saliba
570 AE and Zernecke A. Single-Cell RNA-Seq Reveals the Transcriptional Landscape and
571 Heterogeneity of Aortic Macrophages in Murine Atherosclerosis. *Circ Res*. 2018;122:1661-1674.
572 24. Febbraio M, Podrez EA, Smith JD, Hajjar DP, Hazen SL, Hoff HF, Sharma K and
573 Silverstein RL. Targeted disruption of the class B scavenger receptor CD36 protects against
574 atherosclerotic lesion development in mice. *J Clin Invest*. 2000;105:1049-56.
575 25. Yurdagul A, Jr., Doran AC, Cai B, Fredman G and Tabas IA. Mechanisms and
576 Consequences of Defective Efferocytosis in Atherosclerosis. *Front Cardiovasc Med*. 2017;4:86.
577 26. Hegyi L, Skepper JN, Cary NR and Mitchinson MJ. Foam cell apoptosis and the
578 development of the lipid core of human atherosclerosis. *J Pathol*. 1996;180:423-9.
579 27. Salvayre R, Auge N, Benoist H and Negre-Salvayre A. Oxidized low-density lipoprotein-
580 induced apoptosis. *Biochim Biophys Acta*. 2002;1585:213-21.
581 28. Wick AN, Drury DR, Nakada HI and Wolfe JB. Localization of the primary metabolic
582 block produced by 2-deoxyglucose. *J Biol Chem*. 1957;224:963-9.
583 29. Kim K, Shim D, Lee JS, Zaitsev K, Williams JW, Kim KW, Jang MY, Seok Jang H, Yun
584 TJ, Lee SH, Yoon WK, Prat A, Seidah NG, Choi J, Lee SP, Yoon SH, Nam JW, Seong JK, Oh
585 GT, Randolph GJ, Artyomov MN, Cheong C and Choi JH. Transcriptome Analysis Reveals
586 Nonfoamy Rather Than Foamy Plaque Macrophages Are Proinflammatory in Atherosclerotic
587 Murine Models. *Circ Res*. 2018;123:1127-1142.

588 30. Liang J, Cao R, Wang X, Zhang Y, Wang P, Gao H, Li C, Yang F, Zeng R, Wei P, Li D,
589 Li W and Yang W. Mitochondrial PKM2 regulates oxidative stress-induced apoptosis by
590 stabilizing Bcl2. *Cell Res*. 2017;27:329-351.
591 31. Chen J, Xie J, Jiang Z, Wang B, Wang Y and Hu X. Shikonin and its analogs inhibit
592 cancer cell glycolysis by targeting tumor pyruvate kinase-M2. *Oncogene*. 2011;30:4297-306.
593 32. Craig EA. Hsp70 at the membrane: driving protein translocation. *BMC Biol*. 2018;16:11.
594 33. D'Silva P, Liu Q, Walter W and Craig EA. Regulated interactions of mtHsp70 with
595 Tim44 at the translocon in the mitochondrial inner membrane. *Nat Struct Mol Biol*.
596 2004;11:1084-91.
597 34. Wu PK, Hong SK, Starenki D, Oshima K, Shao H, Gestwicki JE, Tsai S and Park JI.
598 Mortalin/HSPA9 targeting selectively induces KRAS tumor cell death by perturbing
599 mitochondrial membrane permeability. *Oncogene*. 2020;39:4257-4270.
600 35. Wadhwa R, Sugihara T, Yoshida A, Nomura H, Reddel RR, Simpson R, Maruta H and
601 Kaul SC. Selective toxicity of MKT-077 to cancer cells is mediated by its binding to the hsp70
602 family protein mot-2 and reactivation of p53 function. *Cancer Res*. 2000;60:6818-21.
603 36. Mailloux RJ. Teaching the fundamentals of electron transfer reactions in mitochondria
604 and the production and detection of reactive oxygen species. *Redox Biol*. 2015;4:381-98.
605 37. Gerlach BD, Ampomah PB, Yurdagul A, Jr., Liu C, Lauring MC, Wang X, Kasikara C,
606 Kong N, Shi J, Tao W and Tabas I. Efferocytosis induces macrophage proliferation to help
607 resolve tissue injury. *Cell Metab*. 2021;33:2445-2463 e8.
608 38. Zhang S, Weinberg S, DeBerge M, Gainullina A, Schipma M, Kinchen JM, Ben-Sahra I,
609 Gius DR, Yvan-Charvet L, Chandel NS, Schumacker PT and Thorp EB. Efferocytosis Fuels
610 Requirements of Fatty Acid Oxidation and the Electron Transport Chain to Polarize
611 Macrophages for Tissue Repair. *Cell Metab*. 2019;29:443-456 e5.
612 39. Sena LA and Chandel NS. Physiological roles of mitochondrial reactive oxygen species.
613 *Mol Cell*. 2012;48:158-67.
614 40. Yu T, Robotham JL and Yoon Y. Increased production of reactive oxygen species in
615 hyperglycemic conditions requires dynamic change of mitochondrial morphology. *Proc Natl*
616 *Acad Sci U S A*. 2006;103:2653-8.
617 41. Shirai T, Nazarewicz RR, Wallis BB, Yanes RE, Watanabe R, Hilhorst M, Tian L,
618 Harrison DG, Giacomini JC, Assimes TL, Goronzy JJ and Weyand CM. The glycolytic enzyme

619 PKM2 bridges metabolic and inflammatory dysfunction in coronary artery disease. *J Exp Med*.
620 2016;213:337-54.
621 42. Doddapattar P, Dev R, Ghatge M, Patel RB, Jain M, Dhanesha N, Lentz SR and Chauhan
622 AK. Myeloid Cell PKM2 Deletion Enhances Efferocytosis and Reduces Atherosclerosis. *Circ*
623 *Res*. 2022;130:1289-1305.
624 43. Kumar A, Gupta P, Rana M, Chandra T, Dikshit M and Barthwal MK. Role of pyruvate
625 kinase M2 in oxidized LDL-induced macrophage foam cell formation and inflammation. *J Lipid*
626 *Res*. 2020;61:351-364.
627 44. Alves-Filho JC and Palsson-McDermott EM. Pyruvate Kinase M2: A Potential Target for
628 Regulating Inflammation. *Front Immunol*. 2016;7:145.
629 45. Zhao X, Zhu Y, Hu J, Jiang L, Li L, Jia S and Zen K. Shikonin Inhibits Tumor Growth in
630 Mice by Suppressing Pyruvate Kinase M2-mediated Aerobic Glycolysis. *Sci Rep*. 2018;8:14517.
631 46. Huang B, Wang Q, Jiang L, Lu S, Li C, Xu C, Wang C, Zhang E and Zhang X. Shikonin
632 ameliorated mice colitis by inhibiting dimerization and tetramerization of PKM2 in
633 macrophages. *Front Pharmacol*. 2022;13:926945.
634 47. May RC and Machesky LM. Phagocytosis and the actin cytoskeleton. *J Cell Sci*.
635 2001;114:1061-77.
636 48. Rouyere C, Serrano T, Fremont S and Echard A. Oxidation and reduction of actin:
637 Origin, impact in vitro and functional consequences in vivo. *Eur J Cell Biol*. 2022;101:151249.
638

FIGURES WITH FIGURE LEGENDS

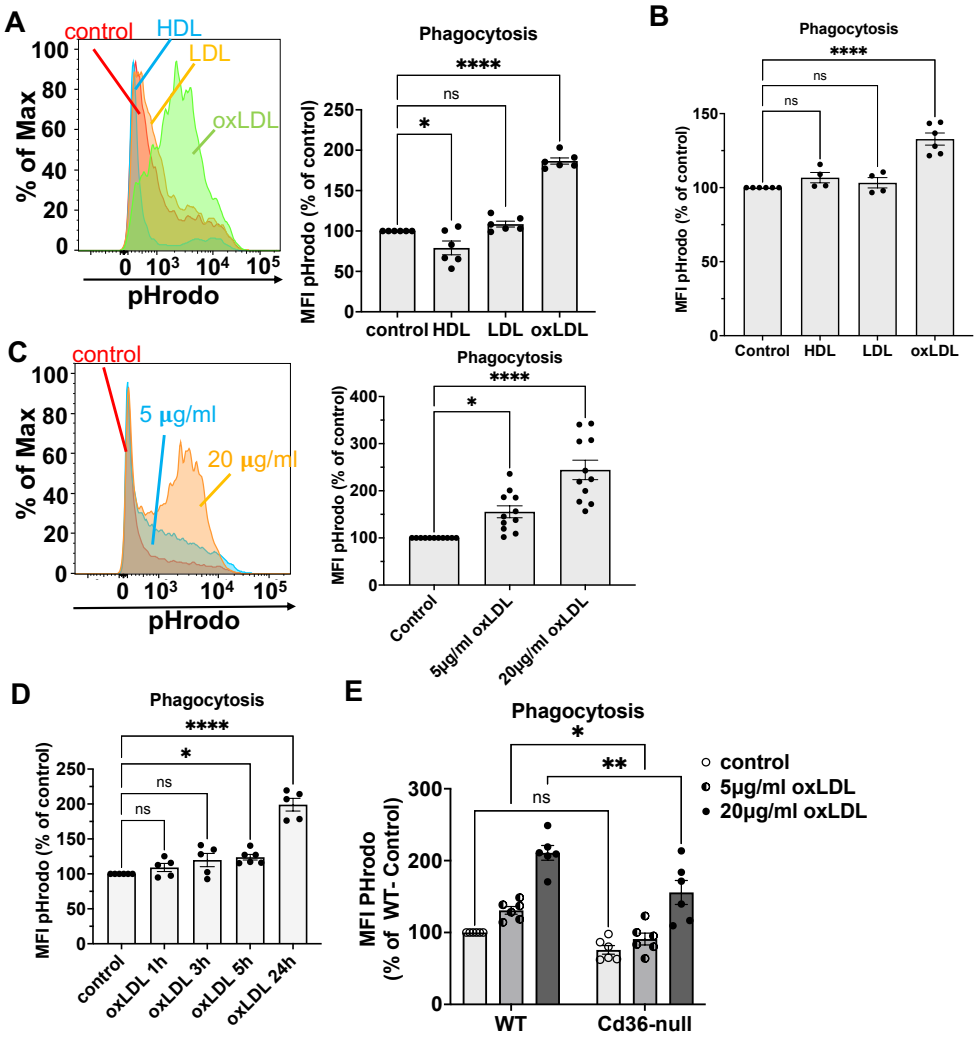

Figure 1. Oxidized LDL (oxLDL) stimulates CD36-dependent phagocytosis in macrophages. **A**, Examples of histograms of pHrodo fluorescence in WT peritoneal macrophages pre-treated with 20 μg/ml HDL or LDL or oxLDL for 24 h, followed by pHrodo-conjugated *E. coli* co-incubation for 30 min and flow cytometry analysis. Mean fluorescence intensity (MFI) of pHrodo was quantified and shown in the bar graph; n=3 per group. **B**, HMDMs were pre-treated with 50 μg/ml HDL or LDL or oxLDL for 24h before phagocytosis assay. MFIs are shown in the bar graph; n=3 per group. **C**, Examples of histograms of pHrodo fluorescence in WT peritoneal macrophages pre-treated with 5 or 20 μg/ml of oxLDL for 24 h before phagocytosis assay. MFIs are shown in the bar graph; n=4 per group. **D**, WT peritoneal macrophages pre-treated with 20 μg/ml oxLDL for indicated time before phagocytosis assay. The pHrodo MFI was quantified and shown in the bar graph; n=3 per group. **E**, WT, or *Cd36*-null peritoneal macrophages were pre-treated with 5 or 20 μg/ml oxLDL for 24 h before phagocytosis assay. The pHrodo MFI was quantified and shown in the bar graph; n=3 per group. Max, maximum fluorescence intensity.

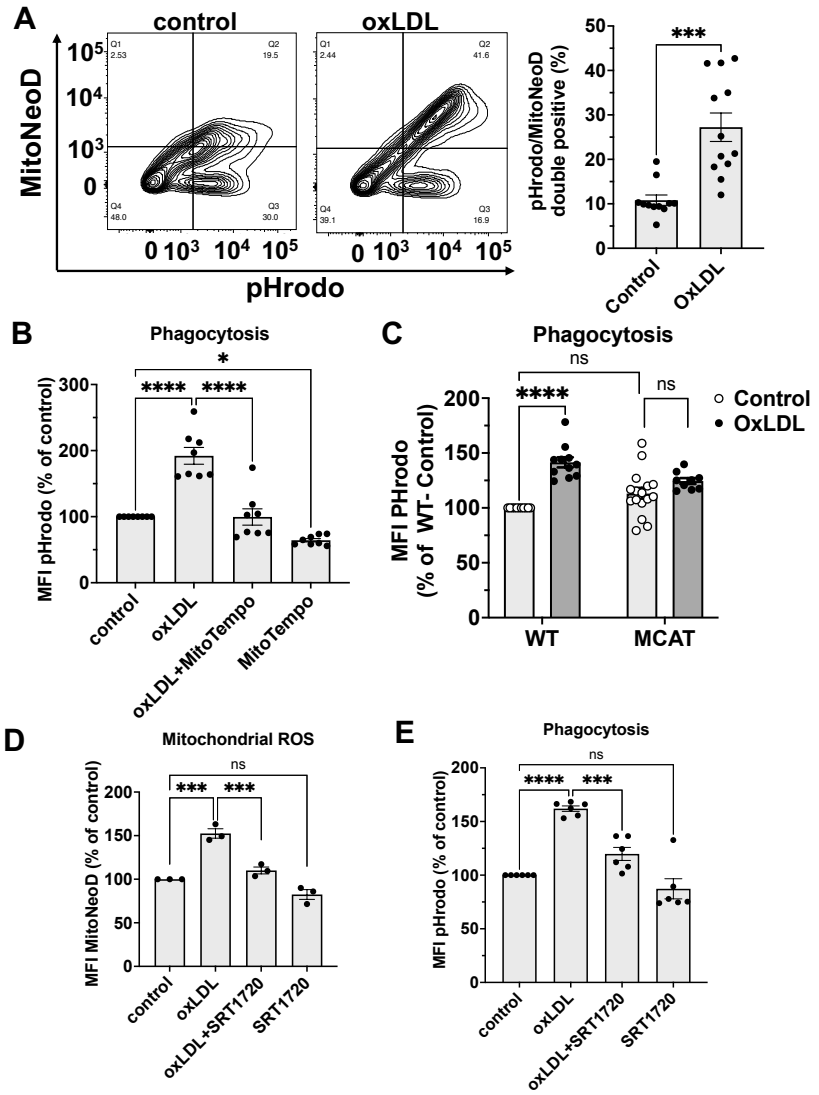

Figure 2. OxLDL-induced phagocytosis is dependent on mitochondrial reactive oxygen species (mtROS). A, Examples of contour plots showing MitoNeoD and pHrodo signals from WT peritoneal macrophages pre-treated with 20 μg/ml oxLDL for 24 h. The percentage of MitoNeoD/pHrodo double positive populations was quantified and shown in the bar graph; n=3-5 per group. **B**, WT peritoneal macrophages pre-treated with 20 μg/ml oxLDL for 24 h, followed by 1mM MitoTEMPO incubation for 1 h before phagocytosis assay. The pHrodo MFI was quantified and shown in the bar graph; n=3 per group. **C**, WT, or MCAT peritoneal macrophages pre-treated with 20 μg/ml oxLDL for 5 h before phagocytosis assay. The pHrodo MFI was quantified and shown in the bar graph; n=4-5 per group. **D**, WT peritoneal macrophages pre-treated with 20 μg/ml oxLDL for 24 h, followed by 20 μM SRT1720 for 1 h before MitoNeoD staining. The MitoNeoD MFI was quantified and shown in the bar graph; n=3 per group. **E**, The same treatment as in D before phagocytosis assay. The pHrodo MFI was quantified and shown in the bar graph; n=3 per group.

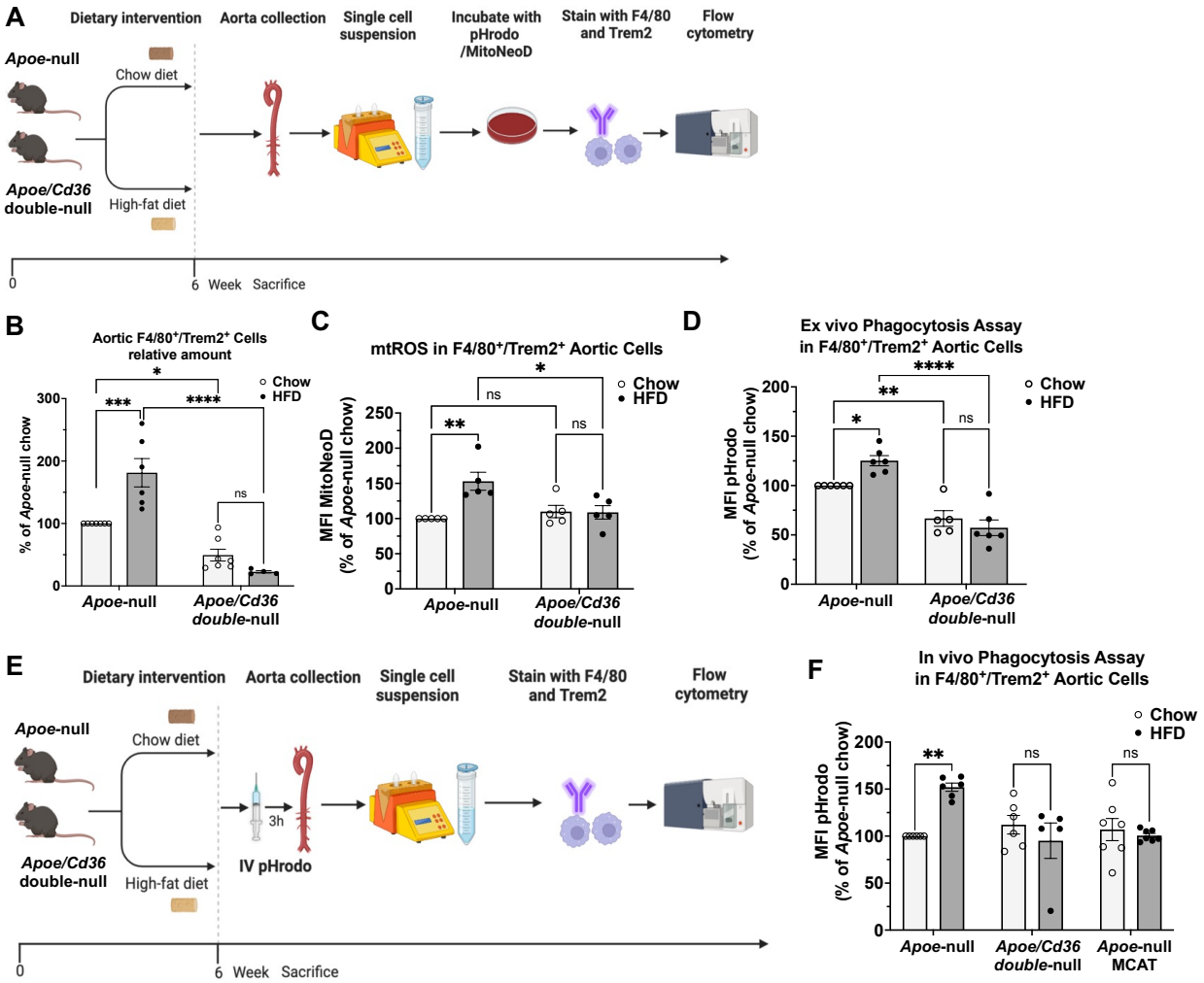

Figure 3. Aortic F4/80$^+$/Trem2$^+$ macrophages show increased mtROS and phagocytosis efficiency dependent on CD36 during the initiation stages of atherosclerosis. A, a diagram of the *ex vivo* mtROS and phagocytosis assay. **B**, Total amount of aortic F4/80$^+$/Trem2$^+$ macrophages were quantified and shown in the bar graph; n=4-7 individual mice per group. **C**, MitoNeoD MFI was quantified in aortic F4/80$^+$/Trem2$^+$ macrophages and shown in the bar graph; n=5 individual mice per group. **D**, pHrodo MFI was quantified in aortic F4/80$^+$/Trem2$^+$ macrophages and shown in the bar graph; n=5-6 individual mice per group. **E**, a diagram of the *in vivo* phagocytosis assay. **F**, pHrodo MFI was quantified in aortic F4/80$^+$/Trem2$^+$ macrophages and shown in the bar graph; n=5-7 individual mice per group.

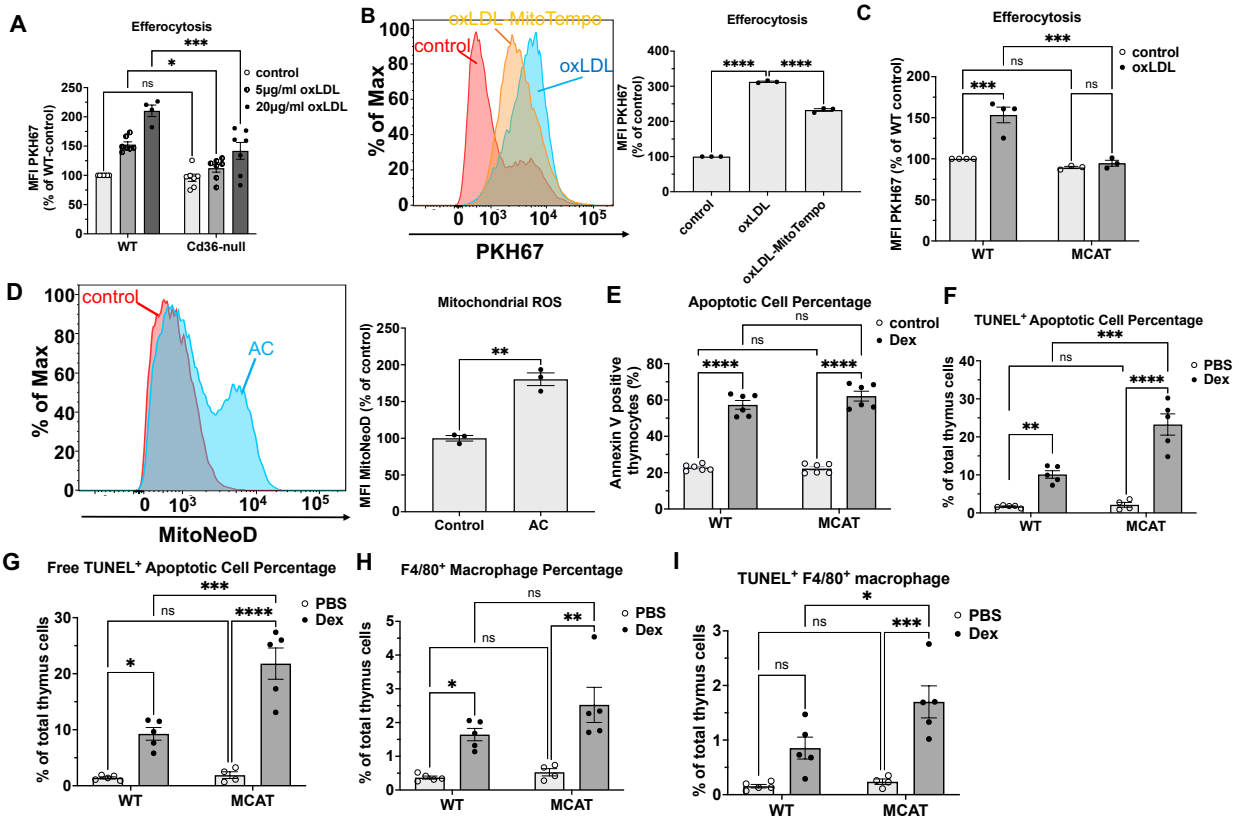

Figure 4. OxLDL stimulates efferocytosis, which is dependent on CD36 and mtROS. A, WT, or *Cd36*-null peritoneal macrophages were pre-treated with 5 or 20 μg/ml oxLDL for 24h before co-incubation with PKH67-labeled apoptotic foam cells for 15 min (efferocytosis assay). The PKH67 MFI was quantified and shown in the bar graph; n=3-4 per group. **B**, Examples of histograms of PKH67 fluorescence in WT peritoneal macrophages pre-treated with 20 μg/ml oxLDL or in combination with 1mM MitoTEMPO for 24 h before efferocytosis assay. The PKH67 MFI was quantified and shown in the bar graph; n=3 per group. **C**, WT, or MCAT peritoneal macrophages pre-treated with 20 μg/ml oxLDL for 5 h before efferocytosis assay. The PKH67 MFI was quantified and shown in the bar graph; n=3-4 per group. **D**, Examples of histograms of MitoNeoD fluorescence in WT peritoneal macrophages co-incubated with AC for 30 min, followed by MitoNeoD staining. The MitoNeoD MFI was quantified and shown in the bar graph; n=3 per group. **E**, WT, or MCAT thymocytes were treated with 5 μg/ml dexamethasone (Dex) for 20 h in vitro, followed by PE-conjugated Annexin V staining for PS-exposed AC. AC rates among all thymocytes were quantified by flow cytometry and shown in the bar graph; n=6 per group. **F-I**, WT, or MCAT mice were peritoneally injected with dexamethasone (250 μg in 1 ml PBS per mouse). 20 h later, mice were sacrificed, and thymocytes were stained with TUNEL and anti-F4/80 antibody, followed by flow cytometry analysis. The percentages of total TUNEL$^+$ cells (**F**), free TUNEL$^+$ cells (TUNEL$^+$/F4/80$^-$) (**G**), total F4/80$^+$ macrophages (**H**), and TUNEL$^+$/F4/80$^+$ efferocytes (**I**) were quantified and shown in the bar graph. Max, maximum fluorescence intensity.

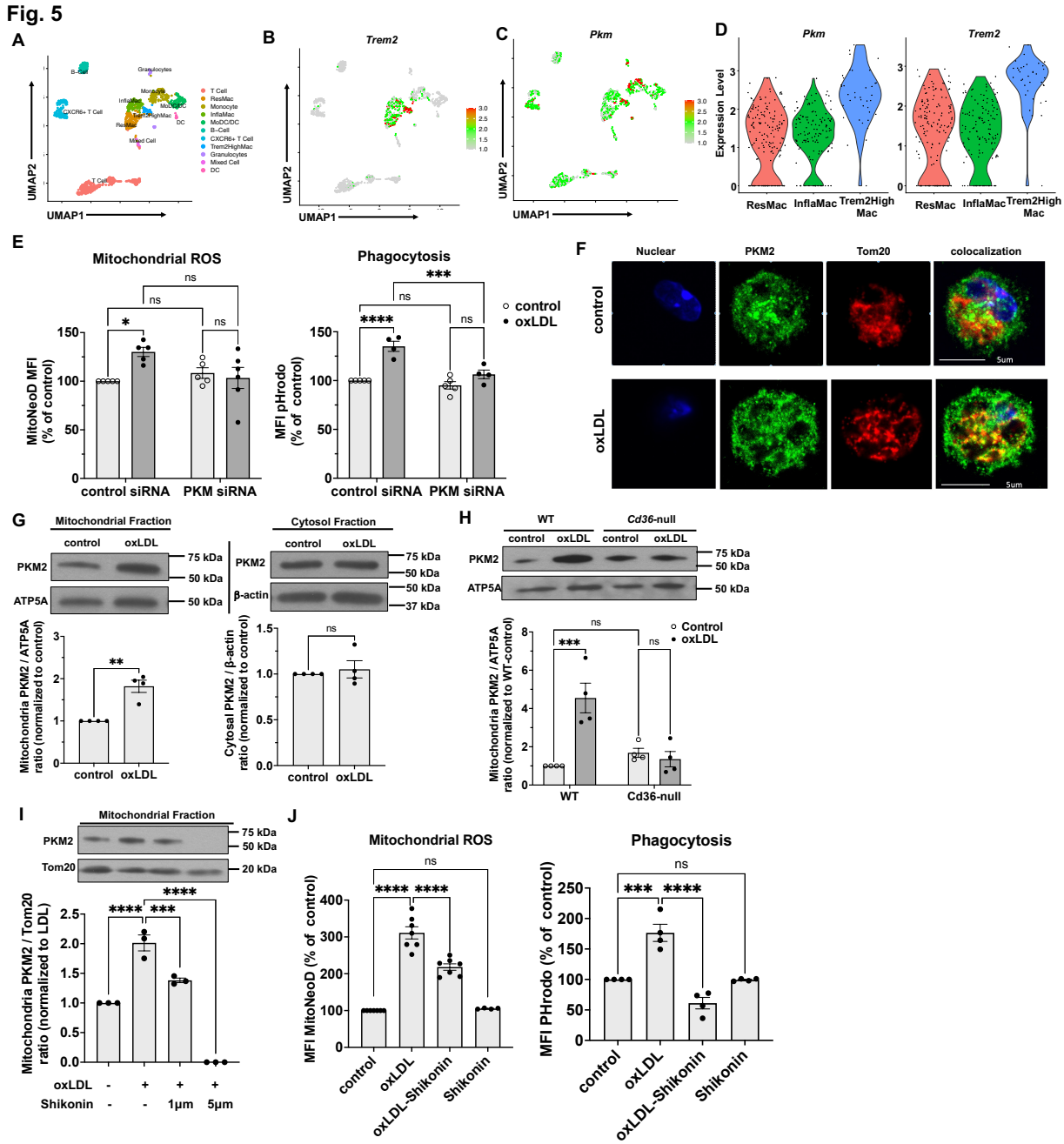

Figure 5. Pyruvate kinase M2 (PKM2) translocate to the mitochondria, promoting mtROS and phagocytosis in macrophages. A-D, Mouse scRNA-seq data were re-analyzed from a previous publication[23]. Uniform manifold approximation and projection (UMAP) representation of 11 aortic CD45^{+} immune cell clusters were shown in **A**. Trem2 gene expression pattern (**B**) and Pkm gene expression pattern (**C**) were shown in the UMAP. **D**, Violin plots show the Pkm and Trem2 expression distribution among aortic macrophage subpopulations. ResMac: resident macrophages; InflaMac: inflammatory macrophages. **E**, HMDMs transfected with PKM siRNA were treated with 50 μg/ml oxLDL for 24 h before subjected to mtROS assay (left panel) or phagocytosis assay (right panel). MFI was quantified and shown in the bar graph; n=4-5 per group. **F**, Representative confocal images of macrophages immunostained for PKM2 (green) and Tom20

713 (red). Nuclei were stained by DAPI (blue). Scale bar: 5 μm. **G**, HMDMs treated with 20 μg/ml
714 LDL (control) or oxLDL for 3 h were lysed, subjected to cell fractionation into mitochondrial and
715 cytosol fractions. PKM2 and ATP5A (mitochondria fraction loading control) blot images from
716 mitochondrial fractions were shown on the left. PKM2 and β-actin (cytosol fraction loading
717 control) blot images from cytosol fractions were shown on the right. Images were quantified,
718 normalized to each loading control, and expressed as fold change of control. n=4 per group. **H**,
719 WT or *Cd36*-null peritoneal macrophages treated with 20 μg/ml LDL (control) or oxLDL for 3 h
720 and then processed as in G. Mitochondrial fractions were immunoblotted for PKM2 and ATP5A
721 and blot images were shown. Images were quantified, normalized, and expressed as fold change
722 of control. n=4 per group. **I**, WT macrophages treated with 20 μg/ml oxLDL or pre-treated 1 or 5
723 μM shikonin before addition of oxLDL, incubating for 3 h, and then processed as in G.
724 Mitochondrial fractions were immunoblotted for PKM2 and Tom20 and blot images were shown.
725 Images were quantified and expressed as fold change of control. n=3 per group. **J**, WT
726 macrophages pre-treated with 20 μg/ml oxLDL or in combination with 1 μM shikonin for 24 h
727 before mtROS or phagocytosis assay. The MitoNeoD (left) or pHrodo (right) MFI was quantified
728 and shown in the bar graph; n=3-4 per group.
729

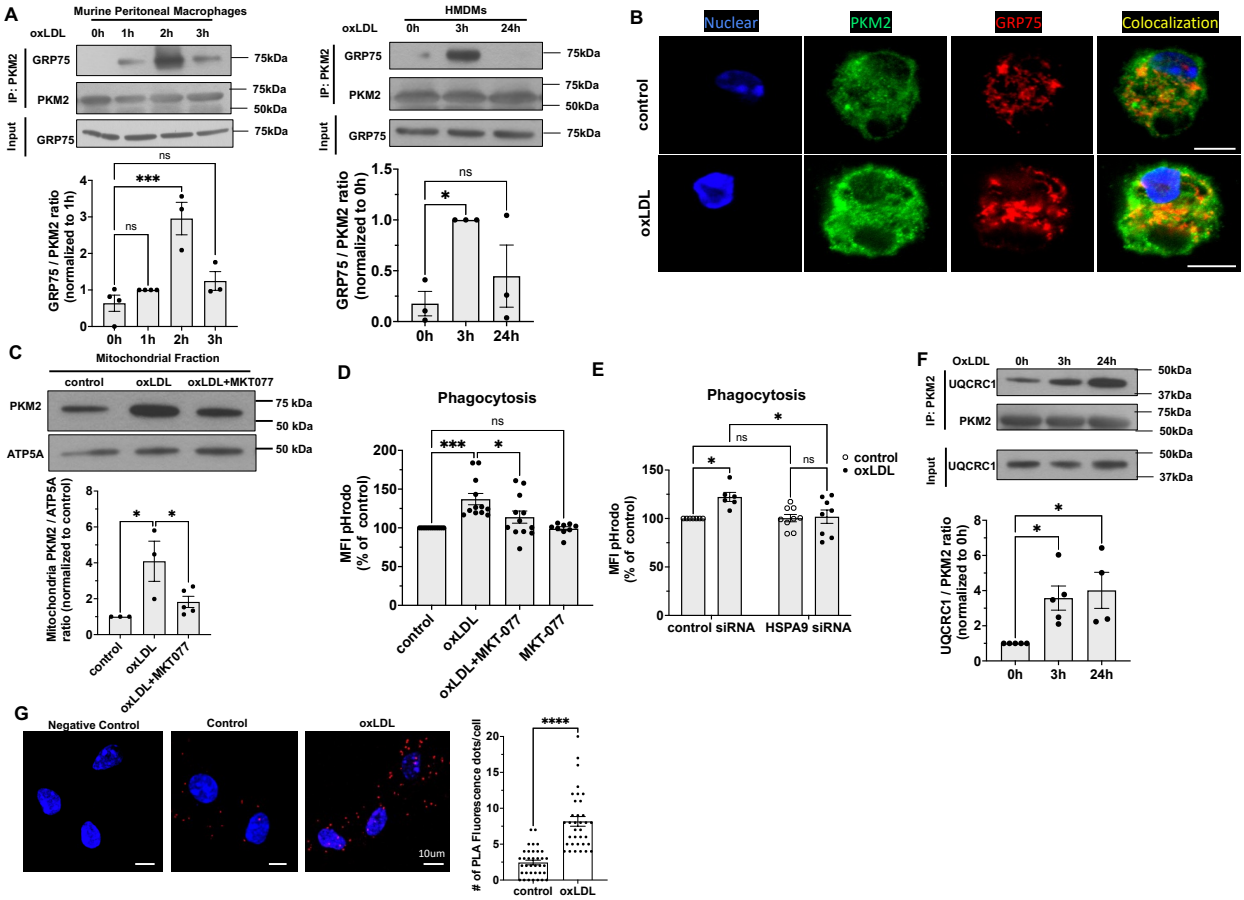

Figure 6. GRP75 mediates PKM2 translocation to the mitochondria, where it interacts with the ETC Complex III. A, Murine peritoneal macrophages (left) or HMDMs (right) were treated with 20 μg/ml oxLDL for indicated time periods before cell lysates were IP with anti-PKM2. Representative Western blot images of GRP75 and PKM2 from PKM2 precipitates and GRP75 from total cell lysates (Input) were shown. Images were quantified and expressed as fold change of 1 h. n=3 per group. **B**, Representative confocal images of macrophages immunostained for PKM2 (green) and GRP75 (red). Nuclei were stained by DAPI (blue). Scale bar: 5 μm. **C**, WT macrophages were treated with 20 μg/ml oxLDL or pre-treated with 0.1 μM MKT077 before addition of oxLDL, incubating for 3 h before cell fractionation. Mitochondrial fractions were immunoblotted for PKM2 and ATP5A and blot images were shown. Images were quantified and expressed as fold change of control. n=3-5 per group. **D**, 24-h treatement of oxLDL or in combination with MKT077 as in C before phagocytosis assay. pHrodo MFI was quantified and shown in the bar graph; n=3-4 per group. **E**, HMDMs transfected with HSPA9 siRNAs were treated with 50 μg/ml oxLDL for 24 h before subjected to phagocytosis assay. MFI was quantified and shown in the bar graph; n=3-5 per group. **F**, WT peritoneal macrophages treated with 20 μg/ml oxLDL for indicated time periods before cell lysates were IP with anti-PKM2. Representative Western blot images of UQCRC1 and PKM2 from PKM2 precipitates and UQCRC1 from total cell lysates (Input) were shown. Images were quantified and expressed as fold change of 0h (control). n=4-5 per group. **G**, Representative confocal images from *in-situ* proximity ligation assay (PLA) show enhanced PKM2/UQCRC1 interaction with or without 20 μg/ml oxLDL 24 h

751 treatment. The PLA signals (red fluorescence dots) were quantified and shown in the bar graph.
752 The PLA assay without primary antibody addition serves as a negative control. Scale bar: 10 μm.
753

754 **NOVELTY AND SIGNIFICANCE**

755 What is known?

756 • The phagocytosis of apoptotic cells by macrophages is impaired in the advanced stage of
757 atherosclerosis. However, the phagocytosis capacity and the underlying regulatory
758 mechanisms during the initiation stage of atherosclerosis remain poorly understood.

759 • OxLDL binds to its receptor CD36 and induces reactive oxygen species (mtROS) from the
760 mitochondria, promoting pro-atherogenic phenotypes in macrophages and atherosclerosis
761 progression in mouse models.

762 • The pyruvate kinase muscle 2 (PKM2) facilitates diet-induced atherosclerosis in mice, and is
763 also upregulated and associated with increased mtROS in monocytes/macrophages from
764 patients with coronary artery disease.

765 What new information does this article contribute?

766 • OxLDL/CD36 axis upregulates phagocytosis efficiency in macrophages through mtROS.

767 • Aortic foamy macrophages display CD36-dependent increased phagocytosis efficiency and
768 mtROS levels in the initiation stage of diet-induced atherosclerosis in mice.

769 • Mechanistically, oxLDL/CD36 axis promotes the translocation of a cytosolic enzyme PKM2
770 to mitochondria, facilitated by a chaperone protein GRP75. Mitochondrial PKM2 translocation
771 is responsible for mtROS induction and upregulation in phagocytosis.

772 Macrophage phagocytosis is critical to maintaining tissue homeostasis by removing pathogens,
773 apoptotic cells and cell debris. However, unlimited stimulation of phagocytosis lead to metabolic
774 defects and lipid accumulation, which may facilitate foam cell formation and initiation of
775 atherosclerosis. In this study, we report that the foam cell-inducing ligand oxLDL upregulates
776 phagocytosis efficiency in macrophage through CD36-mtROS pathway. Through genetic silencing,
777 transgenic strategy, and pharmacological inhibition combined with *in vitro, ex vivo* and *in vivo*
778 approaches, we found that oxLDL/CD36 axis promotes the translocation of PKM2 to mitochondria,
779 which is responsible for mtROS production and phagocytosis promotion. Our findings define a
780 novel regulatory mechanism of phagocytosis in proatherogenic macrophages, which may provide
781 new therapeutic strategies to balance lipid metabolism and reduce foam cell formation.